Density functional study of self-diffusion along an isolated screw dislocation in fcc Ni

Luke J. Wirth,[1,2] Amir A. Farajian,[1] and Christopher Woodward[2,*]

[1]*Department of Mechanical and Materials Engineering, Wright State University, Dayton, Ohio 45435-0001, USA*

[2]*Materials and Manufacturing Directorate, Air Force Research Laboratory, Wright Patterson Air Force Base, Dayton, Ohio 45433-7817, USA*

(Received 16 October 2018; revised manuscript received 29 January 2019; published 14 March 2019)

Vacancy-mediated diffusion along dislocations, often referred to as pipe diffusion, can contribute to creep deformation of metals in many engineering applications. This process is studied along an $\frac{a}{2}\langle 1\bar{1}0\rangle$ screw dislocation in fcc Ni using a density functional theory approach. An accurate geometrical configuration of the screw dislocation core, dissociated into Shockley partial dislocations and separated by a stacking fault, was previously derived using a lattice Green's function technique. Activation energies and jump frequencies are calculated for atom-vacancy exchanges that contribute to diffusion around and along one of the partial cores. This analysis reveals the significant role of the sites within the compressive component of the dislocation, the dominant contribution of the hops around the screw geometry rather than directly along the dislocation line, and the importance of including the stacking fault sites. Kinetic Monte Carlo simulations use these energies and frequencies to generate diffusion coefficients that account for correlation effects. Near 80% of the melting temperature T_m, these pipe diffusivities are an order of magnitude higher than those found in fcc regions, and they are eight orders higher at room temperature. Calculations are compared to experimental results and the differences are discussed. While pipe diffusion is unlikely to contribute to isotropic mass flux at low dislocation densities, it will accelerate dislocation mechanisms controlling creep and climb.

DOI: 10.1103/PhysRevMaterials.3.033605

I. INTRODUCTION

Diffusion along dislocation cores in metals (pipe diffusion) can occur at significantly higher rates than diffusion in crystalline regions. The mechanism can have an outsized effect on creep at the macroscopic level, whether due to the diffusion itself or resulting from diffusion-induced grain boundary migration or slip [1]. Creep is a primary contributor to failures in traditional technologies like gas turbines [2] and may be encountered even more frequently in emerging technologies that are engineered at the nanoscale [3]. Pipe diffusion can also be manipulated to produce desirable outcomes, such as in titanium sintering [4].

While pipe diffusion has been discussed in the body of scientific literature for quite some time, only recently have direct observations of the effects been possible. This offers a unique opportunity for advancing our understanding of pipe diffusion by comparing direct simulation with emerging experimental results. One transmission electron microscopy (TEM) study observed pipe diffusion increasing the diffusivity of impurities in aluminum by three orders of magnitude near 600 K [5]. Another, more recent study, captured images of the phenomenon in a superlattice with atomic resolution [6]. Experimental works on nickel have provided Arrhenius parameters for pipe diffusion along an edge dislocation using a surface counting technique at low temperatures [7] and in screw and edge dislocations using a more precise radiography approach [8]. A study using a serial sectioning method suggested that dislocations act as "isolated high-diffusivity pipes" at low temperatures where lattice diffusion is effectively frozen out, and that arrays of dislocations compose regions where diffusion tends to occur at high temperatures [9]. Diffusion in bulk nickel is well represented in both experimental studies using a range of methodologies [10–13] and simulations taking first-principles approaches [14–18]. Numbers generated by these different methodologies cannot always be directly compared, but their findings complement one another in describing how diffusion mechanisms operate. For instance, in many experimental results, behavior of diffusion in fcc regions cannot be isolated from that which takes place along dislocation pipes or in grain boundaries within experimental samples [11]. This is not an issue in simulations where defects can be introduced and modeled independently.

A number of previous studies have simulated pipe diffusion in different materials using various methods. Embedded-atom method (EAM) potentials have been applied to self-diffusion in Al [19] and Mg diffusion in Al-rich Al-Mg [20], and resonant model pseudopotentials have been used to study self-diffusion in Cu [21]. Interstitial Si diffusion at dislocations in Al has been studied using paired quantum and molecular mechanics (QM/MM) with orbital-free density functional theory (DFT) to resolve long-range elastic fields of the dislocations [22].

Here pipe diffusion is modeled along a partial dislocation core in fcc Ni using a fully quantum mechanical approach. An $\frac{a}{2}\langle 1\bar{1}0\rangle$ screw dislocation in fcc Ni, dissociated into Shockley partial dislocations, was prepared using density functional theory and a lattice Green's function embedding method. This technique is well documented [23], and the specific calculations for the screw dislocation in fcc Ni are described

*christopher.woodward@us.af.mil

in the literature [24]. Migration energy barriers and attempt frequencies for many vacancy-atom exchanges that compose pipe diffusion are then calculated within the equilibrium geometry of one of these partial cores. This information is the basis for kinetic Monte Carlo (KMC) simulations of vacancy-mediated mass transport through a dislocation system while accounting for correlation effects. This unique combination of methodologies provides insights into the geometrical and local strain effects that accelerate diffusion in or near the partial dislocations. Of particular interest are the low migration energy barriers around the partial screw dislocation core, on the side of the partial core that contains the compressive side of the edge component of the screw dislocation, and between atomic sites that are adjacent to the partial core and those which lie in the stacking fault.

II. METHODOLOGY

A. Atomic geometry preparation

Calculations were performed using the Vienna *ab initio* simulation package (VASP) [25–28] with generalized gradient approximation projector augmented wave (GGA-PAW) pseudopotentials [29,30]. All calculations were spin polarized with a plane wave basis cutoff of 400 eV, a force tolerance of 0.005 eV/Å, and, following convergence testing, Methfessel-Paxton smearing of 0.25 eV [31]. The spin polarized GGA-PAW approach predicts lattice and elastic constants ($a_0 = 3.5219$ Å, $C_{11} = 2.70$, $C_{12} = 1.56$, $C_{44} = 1.29$ Mbar) that are in good agreement with measured values [32].

In previous work an $\frac{a_0}{2}\langle 1\bar{1}0\rangle$ screw dislocation was relaxed using the two-dimensional (2D) lattice Green's function (LGF) method and the VASP package [24]. This approach produces an isolated dislocation by accounting for the effects of its long-range strain fields on its local geometry [23,33–36]. This leads to an accurate description of the dissociated core structure. The LGF cell consisted of a parallelepiped of 620 atoms, with one periodic unit along the dislocation line, and $20\frac{a_0}{2}\langle 111\rangle$ by $\frac{31}{2}\frac{a_0}{2}\langle 11\bar{2}\rangle$ lattice vectors normal to the line direction. Upon relaxation, the $\frac{a}{2}\langle 1\bar{1}0\rangle$ dislocation dissociates into $\frac{a}{6}\langle 1\bar{2}\bar{1}\rangle$ and $\frac{a}{6}\langle 2\bar{1}1\rangle$ Shockley partial dislocations, which are separated by a stacking fault that is approximately 4**b** wide where the Burgers vector **b** is 2.49 Å. This is in good agreement with the separation width reported by another DFT study using the Peierls-Nabarro approximation as well as the analytic value [37] using anisotropic elasticity theory.

Hexagonal sections around the $\frac{a}{6}\langle 1\bar{2}\bar{1}\rangle$ Shockley partial are extracted from the LGF-generated geometry so that vacancies can be inserted near the dislocation. A representative example of one such section is shown in Fig. 1, where sites that are relaxed following vacancy insertion are shown in white while in the surrounding, shaded region, the sites are fixed. The latter region maintains the structure of the partial dislocation core across relaxations and isolates the core from any effects of proximity to its neighboring periodic images during analysis in VASP. The sites labeled A–E, I, and J in the white region indicate where vacancies could be inserted into the A-centered hexagon in the figure, while the remaining lettered sites indicate where vacancies could be inserted into cells with different centers. Hexagonal cells centered on sites B, C, F, P, and S were also used. The slab of atoms in the figure has a depth of **b** and is repeated four times in the $\langle 1\bar{1}0\rangle$ direction of the dislocation line. So, when periodic boundary conditions are applied in this direction, the single vacancy is separated from its periodic image by 4**b**, and their interactions with one another are assumed to be negligible. Periodic boundary conditions are also applied within the $(1\bar{1}0)$ plane of Fig. 1, such that neighboring hexagonal cells meet at the dashed perimetral line to fill the plane continuously with atoms. Prior to vacancy insertion, positions of atoms at the 76 sites within the relaxation region were optimized within the confines of the fixed boundary. Residual forces were on average $\sim$0.002 eV/Å with a total energy change of $\sim 10^{-4}$ eV/atom on relaxations. One vacancy was inserted in each cell, and the 76 free sites of each cell (now containing 75 atoms and the vacancy) were relaxed again. These configurations were used as initial and final geometries for vacancies moving between adjacent sites. Throughout this process, vacancies were never introduced at sites that bordered a fixed boundary region. Γ-centered $3 \times 3 \times 5$ k meshes were used for these relaxations following convergence testing. Because of the presence of the dislocation and stacking fault in the otherwise fcc geometry, there are geometrical mismatches where the hexagon borders meet one another. Three checks confirmed that the supercells were large enough to confine the significant effects of this mismatch within the fixed boundary region in order to not significantly affect vacancy behavior near the center of the relaxation region [38].

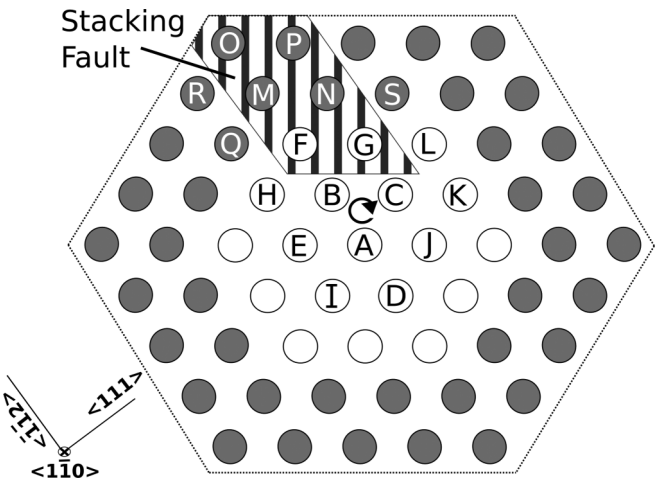

FIG. 1. A cell for modeling atom-vacancy exchanges, containing 244 atomic sites when repeated 4 times in the $\langle 1\bar{1}0\rangle$ direction. One vacancy is introduced at a lettered site near the dislocation, and white atoms are relaxed while shaded ones form a fixed boundary to maintain the dislocation structure. Vacancy migration between any neighboring pair of sites can be studied using two configurations of such a cell, each with a vacancy inserted at one of those sites. Vacancies are never inserted adjacent to the boundary.

B. Vacancy hop rate calculation

Reaction pathways were identified using a nudged elastic band (NEB) method [39–42]. In this approach, i intermediate images discretely represent a minimum energy path (MEP) between two known states of a system. Here these states

are two relaxed configurations of one hexagonal cell with vacancies at adjacent sites, e.g., at sites A and B in Fig. 1. The vacancy migration energy barrier is calculated by

$$E_{m,v0\to vf} = E_{\text{saddle},v0\to vf} - E_{v0}, \tag{1}$$

where $E_{m,v0\to vf}$ is the migration energy for the vacancy to move from site 0 to site f, $E_{\text{saddle},v0\to vf}$ is the NEB-calculated energy of the saddle point of the vacancy transition from site 0 to site f, and E_{v0} is the energy of the cell when the vacancy is at initial site 0. All of these energies are obtained through electronic structure calculations. Each saddle point provides two E_m values, e.g., $E_{m,A\to B}$ and $E_{m,A\leftarrow B}$ where the arrow indicates the direction of the vacancy. These vary as E_{vA} and E_{vB} are not equal for most pairs of sites. An initial configuration of each image is linearly interpolated from the geometries of the cell with its vacancy at initial site 0 and final site f. Then these images are relaxed along NEB forces until they converge along the MEP [38].

For exchanges with migration barriers <0.8 eV, more accurate climbing image NEB (CNEB) simulations rigorously converged on the saddle points of these particularly significant jumps [40]. This threshold was chosen because it includes all vacancy hops between sites that are adjacent to the partial core as well as hops between those sites and sites that lie in the stacking fault. (This energy threshold included 99% of the jumps in later diffusion simulations.)

For each vacancy exchange, a standard NEB calculation was performed to identify a reaction pathway, with the CNEB method optionally following. Variations between NEB and CNEB results were almost always $\lesssim$0.01 eV, so this step was omitted when describing less significant jumps. The CNEB approach would have been necessary to describe all jumps if the diffusion mechanisms in the study were more complicated than vacancies hopping between neighboring sites. A trial that looked at a vacancy exchange between two sites near the partial core that were in each others' second shells of neighbors saw the reported saddle point energy raise by 0.07 eV after the CNEB method was applied. The resultant E_m value of 1.95 eV was high enough that this exchange and others involving comparable interatomic distances were assumed to be energetically unfavorable enough to be negligible. Using one intermediate image was sufficient to study each path [38]. A similar single-image approach has been taken by other authors studying diffusion with similar methodologies [43,44].

These migration energies, along with the Vineyard attempt frequency ν^* [45,46], were then used to calculate the frequency w of each vacancy hop:

$$w = \nu^* \exp\left(-\frac{E_m}{k_B T}\right), \tag{2}$$

$$\nu^* = \frac{\prod_{i=1}^{3} \nu_i}{\prod_{i=1}^{2} \nu_i'}, \tag{3}$$

where ν_i are the vibrational frequencies of an atom at its equilibrium position prior to a hop and ν_i' are its nonimaginary frequencies when it is at the saddle point along the hop. A previous study found that including only frequencies of the hopping atom provides a good approximation of ν^* while limiting error that would otherwise accumulate through inclusion of many frequencies in the product terms [44]. These attempt frequencies were also calculated for hops with energy barriers <0.8 eV, while otherwise the fcc value was used to provide an estimate.

C. Kinetic Monte Carlo calculations

Jump frequencies for all possible vacancy hops within the system were included in a catalog of rate constants for the KMC code, which moves a single vacancy through a system of atomic coordinates according to the Bortz-Kalos-Lebowitz algorithm, also known as the N-fold way [47–49]. A vacancy at a given site has N neighbors within some cutoff distance and a hop rate r to each neighbor [38]. In fcc Ni, the cutoff distance is chosen to be the nearest neighbor distance of 2.49 Å. Within the dislocation cell, it is set slightly higher to accommodate possible vacancy hops within the distorted geometries of the first shells of nearest neighbors of various sites, as discussed later. These neighbors are referred to as "nearby neighbors" of a given site in this work.

At each temperature studied, a vacancy made k random walks through the KMC cell, where each walk consisted of $1000N$ hops with N being the number of atoms in the system. During each walk, one atom in the cell is selected to be a tracer atom, and its behavior is tracked to generate a diffusion coefficient D_{KMC}:

$$D_{\text{KMC}} = \frac{\sum_{i=1}^{k} [z_i(t_i)]^2}{2nt}, \tag{4}$$

where $z_i(t_i)$ is the displacement of the tracer atom over the time t_i elapsed on walk i, n is the dimensionality of the system, and t is the total time of all walks. In the dislocation system, z is the component of displacement in the direction of the dislocation line and $n = 1$. Since the tracer atom relies on the vacancy to move and the vacancy remains in the vicinity of the tracer atom after moving it "forward" in some diffusion direction, correlation effects emerge as the vacancy has some probability of moving the tracer atom "backward," whether on its next hop or after making several hops. One major advantage of the KMC method is that these effects are automatically included, provided that the vacancy's rate catalog is well constructed. A correlation factor that describes this behavior can be calculated as follows [45]:

$$f_i = \frac{[z_i(t_i)]^2}{\sum_{j=1}^{k} \lambda_k^2}, \tag{5}$$

$$f = \langle f_i \rangle, \tag{6}$$

where k is the number of hops that the tracer atom makes during the ith vacancy walk, λ_k is the tracer's displacement during hop k, and $\langle f_i \rangle$ is the mean value of f_i. In the dislocation system, λ_k is the component of displacement along the direction of the dislocation line.

Diffusion coefficients were scaled by the number of vacancies expected within the KMC cell at equilibrium N_v:

$$D = D_{\text{KMC}} N_v, \tag{7}$$

$$N_v = \sum_{i=1}^{N} \exp\left(-\frac{E_{\text{vf},i}}{k_B T}\right), \tag{8}$$

$$E_{\mathrm{vf},i} = (E_{\mathrm{cell},\,vi} + \mu_{\mathrm{Ni}}) - E_{\mathrm{cell}}, \tag{9}$$

$$\mu_{\mathrm{Ni}} = \frac{1}{N} E_{\mathrm{fcc}}, \tag{10}$$

where $E_{\mathrm{vf},i}$ is the energy of vacancy formation at site i, $E_{\mathrm{cell},\,vi}$ is the VASP-calculated electronic energy of a supercell containing a vacancy at site i, μ_{Ni} is the chemical potential of Ni (−5.46 eV/atom), E_{cell} is the energy of the supercell with no vacancy, and N is the number of atoms in a defect free fcc supercell with energy E_{fcc}. In Eq. (9) the dislocation, stacking fault, and same fixed boundary region are present in both of the supercell configurations that have $E_{\mathrm{cell},\,vi}$ and E_{cell}. The energy difference that is not accounted for by the chemical potential of the missing Ni atom is therefore the energy of vacancy formation at site i [50].

$E_{\mathrm{vf},i}$ at a given site could fluctuate <0.02 eV when a particular vacancy was considered in different hexagonal cells. This effect arose because different hexagonal cells contained different proportions of the three possible types of sites: partial core adjacent, stacking fault, and fcc. For instance, the cell centered on site F contained more stacking fault sites than the cell centered on site A shown in Fig. 1. These variations could slightly change the volume of the relaxation region. In these cases, the lowest $E_{\mathrm{vf},i}$ value that was calculated for a particular site i was used in later calculations, under the assumption that the higher energies corresponded to vacancies and their surrounding atoms being unable to completely relax because of the boundary conditions of the specific hexagonal cell choice. Differences in migration energies from different cells were similarly <0.02 eV. This is within the predicted margin of error given that DFT calculations are generally accurate to approximately 2–3 meV/atom.

D. KMC supercell geometry

KMC simulations of diffusion in the partial dislocation core took place in a cell generated from atomic coordinates, derived by the LGF approach, repeated ten times along the dislocation line, and with periodic boundary conditions applied in the direction of the dislocation line. This cell is depicted in Fig. 2. Migration energy barrier calculations informed the choices of these sites, as is discussed in Sec. III B. Simulations in the 350-atom dislocation core cells consisted of at least 100 000 walks or about 3×10^{10} steps. Separate simulations of an 864-atom fcc Ni cell were also performed with 4000 walks or about 3×10^{9} steps. The fcc cell was larger to provide the vacancy with enough separation from its images in neighboring supercells in all three dimensions in order to more accurately describe correlation effects. Fewer total steps were required for these results to converge due to symmetry.

In all cases, tracer atoms and vacancies were inserted randomly throughout the cell. This was done to avoid biased sampling of particular diffusion pathways. Each simulation was tested for convergence through an analysis of the squared displacement of the tracer atom on each walk. Calculating the standard error $s/\sqrt{(k)}$ of that displacement, where s is the standard deviation and k is the number of walks, confirms that it was less than 1% of the mean squared displacement at each temperature.

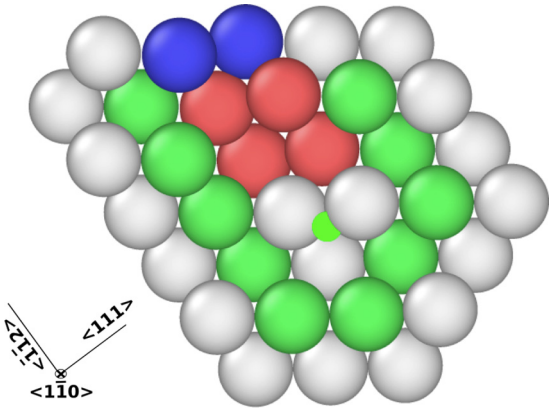

FIG. 2. View of the cell used for the KMC simulation normal to the dislocation line, visualized in and with the dislocation core identified using the dislocation extraction algorithm (DXA) of the Open Visualization Tool OVITO [51–53]. White sites surround the partial dislocation core (near core), red sites lie in the stacking fault, and green sites are surrounding fcc. The white perimeter sites compose an fcc boundary condition region and the dark blue sites indicate a stacking fault boundary condition region.

Upon initialization of a KMC simulation, nearby neighbors of all potentially vacant sites are identified and jump rates to each of them are calculated. An example of the possible vacancy destinations from an "A" site hop, viewed from within the plane normal to the dislocation line, is illustrated in Fig. 3. Hops into the perimeter boundary region of Fig. 2 are assumed to behave like those in the pure fcc case. Upon a vacancy

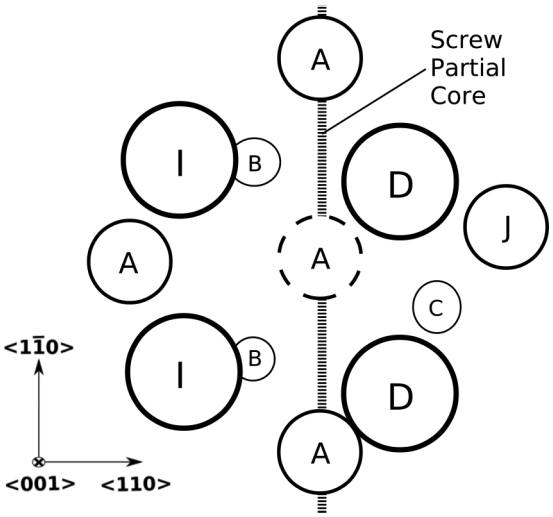

FIG. 3. In-plane view of possible vacancy hop destinations when a vacancy is at the central A site. Perspective is exaggerated to indicate distribution of the sites in the ⟨001⟩ direction. Atomic sites are shifted from their fcc positions because of the partial screw dislocation, which runs vertically between the A, B, and C sites. Eleven nearby neighbors are depicted rather than the 12 nearest neighbors that a normal fcc site would have. In this example, the 12th nearest site is a second "C" atom with a migration energy barrier that is high enough that the probability of the vacancy hopping to that site is negligible.

entering this region, it is randomly returned to another site that borders the boundary. This allows the model to account for the effects of a vacancy randomly wandering from and to the core, assuming this is an isotropic process. If the vacancy hopped along the stacking fault in the direction of the other partial core, e.g., from an M site to an O site in Fig. 1, it was returned to an N site as though it had migrated from the equal and opposite counterpart partial core. Vacancy diffusion from one partial to the other was also assumed to be isotropic. Results are scaled with the equilibrium vacancy concentration term of Eq. (7), and effects of vacancy buildup or depletion are omitted as only one isolated vacancy is ever considered. This assumption is validated by the equilibrium concentration of vacancies at the highest temperature of 1400 K being about one per 230 KMC cells or 4×10^4 sites.

III. RESULTS AND DISCUSSION

A. Electronic structure calculations

Vacancy migration energy barriers E_m between adjacent sites, which were used as input for the KMC simulations, are provided in Fig. 4(a). There they are organized by intersite distance and categorized by the type of site that the vacancy hops from. Each intersite distance is defined as the distance between a pair of atoms in the LGF-produced geometry, before any vacancies are inserted. The distorted geometry near the dislocation causes the nearby intersite distances to vary around the 2.49 Å distance seen in defect free fcc Ni. Many of the migration energies near the dislocation core and in the stacking fault are significantly less than the fcc value, and a trend towards restoring the fcc behavior is observed as these distortions diminish. Increasing this distance does not have a one-to-one correspondence with increases in migration energy for two reasons. The geometries of atoms that surround two pairs can be different depending on location. For example, an F site has two H-type neighbors that are both 2.47 Å away, but the vacancy migration energy barriers of the two F → H hops are 0.74 and 1.17 eV. Second, the energy of a vacancy hop calculated using Eq. (1) can vary with the direction of the hop between two sites. For instance, an A site has an E neighbor that is 2.51 Å away, and the barrier for that E → A vacancy hop is 1.04 eV even though the intersite distance is greater than that seen in fcc Ni. The counterpart E ← A hop has a barrier of 1.15 eV.

Many of the lowest energies are near the partial core, e.g., a vacancy hopping from an A site to a B site in Fig. 3. In Fig. 4(a), all neighbors of core-adjacent sites within their distorted first shell of nearby neighbors up to 2.63 Å are included, while otherwise a cutoff distance of 2.50 Å is applied. All jumps were analyzed with at least NEB accuracy with the exception of some jumps involving the "R" and "S" sites in the fcc region adjacent to the stacking fault, which were approximated using representative values from nearby exchanges. Beyond the cutoff distance and outside the core region, migration energies become sufficiently large that one can assume their probabilities of occurrence are negligible. Two pairs with intersite distances near 2.6 Å, which both involve a "C" site, are the most extreme examples of this behavior deviating near the core. The tensile side of the edge

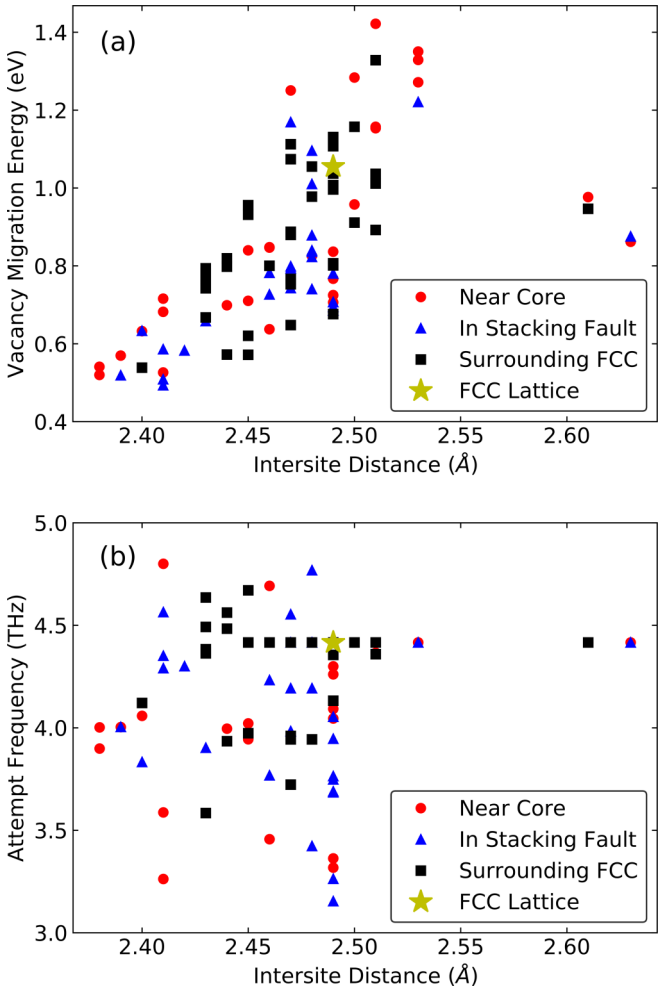

FIG. 4. (a) Migration energy barriers and (b) jump attempt frequencies for all analyzed jumps in the dislocation system. Colors and shapes correspond to the site that the vacancy initiates its hop from. The distance on the x axis is that between atomic sites in the LGF-prepared geometry before a vacancy is introduced.

component of the screw dislocation causes these greater distances to be seen only around this site, and the low migration energy barriers arise from the softened structure of this region, even though the intersite distance is considerably larger than the fcc value.

Since the migration energies contribute to the exponential term in Eq. (2), the energy differences observed throughout this range are the dominant contributors in determining the actual hop rates of the transitions. The attempt frequencies calculated using Eq. (3), which are plotted in Fig. 4(b) for each hop, are mostly near the fcc value of 4.4 THz. These values were only calculated for particularly significant jumps with migration barriers of <0.8 eV. For the most part, these are slightly diminished near the dislocation core and in the stacking fault relative to the value in fcc Ni.

After inserting vacancies at the sites shown in Fig. 1, the vacancy formation energy $E_{\mathrm{vf},i}$ is calculated at each site i using Eq. (9), as shown in Table I. The three most favorable sites for vacancy formation (A, B, and F) are on the side of the cell that contains the compressive side of the edge

TABLE I. Vacancy formation energies (eV) at sites around a partial dislocation core of the $\frac{a}{2}\langle 1\bar{1}0\rangle$ screw dislocation.

Near partial		In fault		Surroundings	
A	1.17	F	1.20	D	1.27
B	1.15	G	1.35	E	1.29
C	1.36	M	1.29	H	1.31
		N	1.34	I	1.30
		O	1.33	J	1.39
		P	1.29	K	1.42
				L	1.41
				Q	1.33
				fcc	1.38

dislocation component of the screw dislocation. Formation of vacancies on that side is energetically favorable as their insertion relieves some of that compression. The directional differences in migration energy, discussed above and shown in Fig. 4(a), are reflected in the varying formation energies at each site.

By summing these values, effective activation energies $Q = E_m + E_{\text{vf}}$ can describe the diffusive behavior of one particular vacancy hop. For instance, $E_{\text{vf},A}$ and the E_m value of the A $\rightarrow$ A hop provide $Q_{\langle 1\bar{1}0\rangle} = 1.94$ eV. This could be applied to describe vacancy diffusion specifically along A sites in that direction. Insertion of these energies into the KMC model is necessary to describe the collective mass transport that depends on many different jumps taking place and interacting in ways that could not be determined *a priori*. Qualitatively, one can note that $Q_{\langle 1\bar{1}0\rangle}$ values near the core are significantly less than the fcc value, which is restored as site distance from the core increases.

B. Kinetic Monte Carlo simulations

Diffusivity in a real material as a function of distance to an isolated dislocation is a continuous function that has a maximum near the core and decays to the bulk value as that distance increases [19]. Practically, an effective dislocation radius is typically assigned such that diffusion within that cross sectional area can be described with one dislocation diffusion coefficient, while outside of that radius, diffusion is assumed to behave like it does in the bulk lattice. Changing the radius of the KMC supercell that contains the dislocation core effectively determines the dislocation density of the KMC simulation, which directly affects the calculated diffusion coefficient. Increasing this radius and therefore the number of fcc sites that lie in the plane that cross sections the dislocation line causes the diffusion coefficient to diminish at a given temperature, both because hops in fcc regions take longer than those that are near the dislocation core and because increasing this area introduces more possibilities for diffusion perpendicular to the dislocation line. Classically, this radius has traditionally been assumed to be well approximated by twice the Burger's vector (~5 Å) [19,54]. A molecular dynamics study of dislocation cores in Al plotted D values as a function of simulation radius and used a curve-fitting technique to identify the radius of their core as approximately 6 Å [19]. In another study Lu and co-workers found

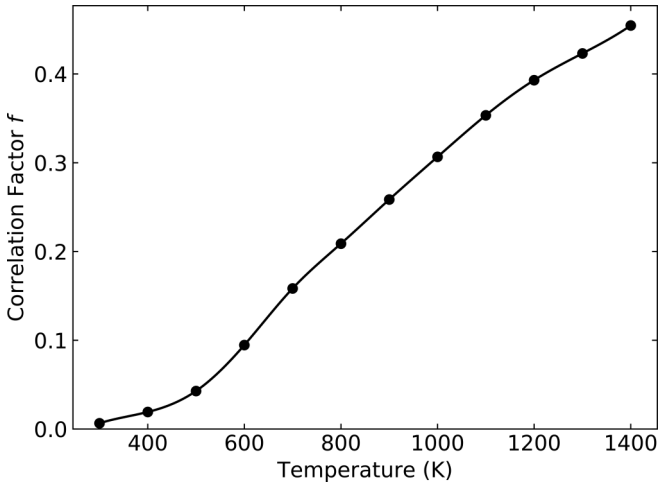

FIG. 5. Correlation factor f in an $\frac{a}{6}\langle\bar{1}2\bar{1}\rangle$ Ni partial screw dislocation core as a function of temperature. Low values at low temperatures are due to the vacancy tending to oscillate along low-energy pathways.

that exchanges involving stacking fault sites are particularly important in describing diffusion near the core [22]. The migration energy results plotted in Fig. 4 suggest that some jumps from the core-adjacent sites to surrounding ones can have high probabilities, for example, $E_{m,A\rightarrow D} = 0.63$ eV. For the pure Ni system, omitting these would hamper the accurate description of vacancy behavior in this region. In another system with vacancies more tightly bound to the dislocation core, this might not be the case. With this in mind, sites under consideration here lie within 2**b** or 4.98 Å of the imaginary line in the $[\bar{1}\bar{1}2]$ direction on the $(1\bar{1}0)$ plane that originates at the partial core and bisects the stacking fault as shown in Fig. 2. This is effectively equivalent to the 5 Å radius assumed for experiments and is also the closest integer multiple of **b** to the value from the MD study; each multiple corresponds to one perimetral layer seen in Fig. 2.

While the primary goal of the KMC model is to calculate diffusion coefficients, one can also extract from it information on the correlation effects that it automatically accounts for as it moves the vacancy through the cell. Correlation factors f for the dislocation core system are calculated using Eq. (6) and plotted as a function of temperature in Fig. 5. These values are consistently lower than the fcc value of 0.78145 [55] due to the vacancy's tendency to oscillate along low-energy pathways between pairs of sites. In an fcc crystal, jumps to any of a vacant site's 12 nearest neighbors are equally energetically favorable. This symmetry causes the vacancy to tend to diffuse through the crystal rather than oscillate along a particular pathway, and also causes the correlation factor to be temperature independent. For the results depicted in Fig. 5, correlation factor values near room temperature particularly pronounce this effect; most of the time, there is not enough kinetic energy in the system to initiate a series of jumps that produces more efficient transport along the dislocation line. As temperature increases, f rises with exponential behavior at the lowest temperatures, adopts a linear trend, and then begins to level off as it approaches the high temperature regime where

TABLE II. A comparison of Arrhenius diffusion parameters for fcc Ni from the current study, another density functional study, and experimental observation.

System	D_0 (m^2/s)	Q (eV)
fcc	4.30×10^{-7}	2.43
Other simulation [18]	4.29×10^{-7}	2.48
Experiment [11]	9.2×10^{-5}	2.88

this analysis stops due to the expected emergence of other diffusion mechanisms [10] and anharmonic effects.

C. Diffusion coefficients

The KMC-generated diffusion coefficients for bulk Ni are in good agreement with those reported by Wu and coworkers using GGA pseudopotentials within VASP [18]. The Arrhenius parameters are listed along with these results in Table II. Minor differences between the two results can be attributed to slight variations in methodology. Also listed are experimental results from one particularly relevant study by Maier [11], which used a relatively accurate direct sectioning technique at comparable temperatures of 813–1193 K while taking measures to omit any contributions from pipe diffusion to their final results.

Multiple factors contribute to the disagreement between the simulation results and the experimental ones. To explain the difference in activation energy, there is an established error in DFT calculations in systems that contain a vacancy. Mattsson and Mattsson have shown that the internal surface area surrounding the vacancy (e.g., a low electron density region) leads to calculated E_{vf} values in Eq. (9) that systematically underestimate experimental values [56]. Using local density approximation (LDA) pseudopotentials can lead to some cancellation of this error (in this case, at the expense of underestimating the lattice constant of Ni), but as Wu *et al.* point out, correctional terms would be needed regardless of the pseudopotential choice to closely match experimental results [18]. They offer correctional shift terms A_{shift} and E_{shift} for D_0 and Q, which have not been applied to the values reported here, but could be applied if desired. One means of bringing the diffusion prefactor into better agreement with experimental results would be to include vibrational contributions to the equilibrium number of vacancies calculated with Eq. (9). These are highly temperature dependent and accurately calculating them in the dislocation system goes beyond the scope of the current study. Recent *ab initio* work investigating this topic in detail for fcc Ni is available in the literature [57].

With this context for interpreting the results in place, diffusion coefficients from the partial dislocation cell are compared with the fcc values. Diffusion coefficient plots for both systems, along with Maier's experimental data for fcc Ni [11], are plotted in Fig. 6. The diffusivities within the partial dislocation system are consistently higher than those found in the fcc system. These values are about one order of magnitude higher at the very highest temperature of 1400 K, and eight orders of magnitude higher near 300 K. For the sake of comparing with other data, Arrhenius parameters have been

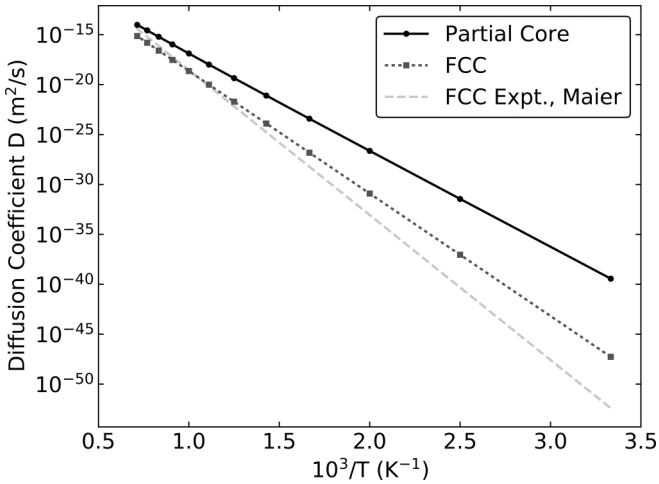

FIG. 6. A comparison of KMC simulation-generated diffusion coefficients in the dislocation cell and in fcc Ni. Experimental data for the fcc case is included from a study that focused on the monovacancy diffusion mechanism in the Ni lattice at comparable temperatures [11].

fit to this pipe diffusion data and are compiled in Table III. Because of the previously discussed temperature effects on correlation factor and hop activity, fits have been made to the entire range as well as in the regions where f displays its approximately prelinear and linear behavior. The traditional $D = D_0 \exp(-Q/k_B T)$ formalism wraps f up in D_0, which is better suited for describing symmetrical systems like the fcc lattice with temperature-independent f values. Regardless, the activation energies of the fits to the dislocation system data are consistently less than the fcc values, which is to be expected given the lowered vacancy migration energy barriers and comparable formation energies in the near-core region. In the low temperature dislocation Arrhenius fit, the diffusion prefactor D_0 is suppressed due to correlation effects. At higher temperatures, Q rises because jumps that require more thermal energy are more active.

By multiplying the diffusion coefficient of the dislocation cell by its area, which is approximately $17\mathbf{b}^2$, the integrated flux (P) can be calculated through the dislocation region. This term, "integrated flux," is in use for consistency with previous literature. For the simulated data, this term is a proportionality constant such that the ratio of flux through different regions, each with some known P_i, can be quickly assessed, and comparisons with experiment can be readily made. The integrated flux was traditionally measured in experiments and used to

TABLE III. Arrhenius diffusion parameters and integrated flux coefficient P_0 for an $\frac{a}{6}\langle \bar{1}2\bar{1} \rangle$ Shockley partial screw dislocation in fcc Ni, obtained by fitting the data at different temperature ranges.

Fit temperature range	D_0 (m^2/s)	P_0 (m^4/s)	Q (eV)
300–1400 K	6.89×10^{-8}	7.26×10^{-26}	1.93
300–700 K	4.28×10^{-8}	4.51×10^{-26}	1.91
800–1400 K	1.28×10^{-7}	1.35×10^{-25}	1.98
Experiment [8,54]	2.6×10^{-4}	6.6×10^{-23}	1.95

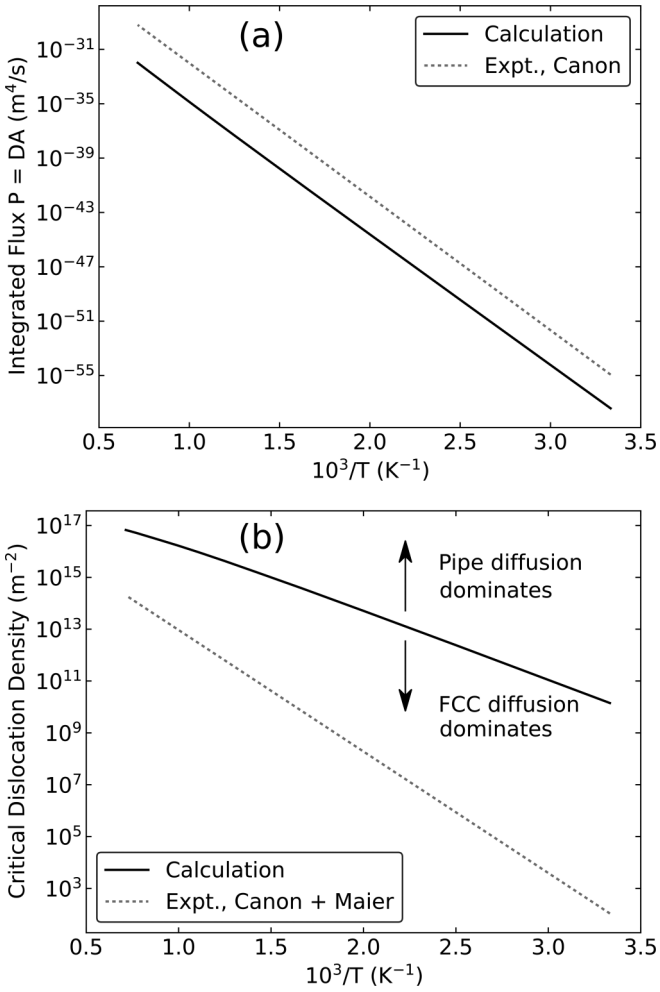

FIG. 7. (a) Integrated flux in the screw dislocation compared to experimental results from a dissociated $\frac{a}{2}\langle 1\bar{1}0\rangle$ screw dislocation in fcc Ni [8]. (b) Critical dislocation densities for pipe diffusion and fcc diffusion to contribute equally to diffusive flux, compared to numbers derived from experimentally determined Arrhenius parameters assuming an effective dislocation area of $\pi(5\ \text{Å})^2$ [8,11].

derive the diffusion coefficient by making an assumption about the area of the diffusion pipe radius as discussed above. This quantity can be fit to temperature to produce an integrated flux coefficient P_0, which is analogous to the Arrhenius prefactor D_0. In Fig. 7(a) the integrated flux through the system is plotted as a function of temperature, along with that which was observed experimentally using radiotracers in dissociated $\frac{a}{2}\langle 110\rangle$ screw dislocations in fcc Ni [8]. (To our knowledge, this is the only experimental work available that specifically considered screw dislocations in Ni.) The calculated and experimental activation energies, which are listed in Table III, are in good agreement with one another with a difference of <0.05 eV, which is significantly less than the deviation between simulated and experimental fcc Ni ($\sim$0.4 eV). Like in the fcc case, the intercept or prefactor of the experimental data is significantly higher than the simulated value, but in the case of the dislocation this difference becomes even more pronounced. One factor that helps to explain this discrepancy is that the experimentally observed screw dislocations were prepared in a grain boundary (GB), and the entropies of vacancy formation S_f in such a geometry can raise D_0. Another theoretical study found S_f/k_B of up to 5.13 at sites in Cu GBs [58]. Given that D_0 is directly proportional to $\exp(S_f/k_B)$, this effect could contribute significantly to an increase in the equilibrium vacancy concentration. Additionally, the experiment operated at 873–1243 K and its findings were extrapolated to the entire temperature range.

In a deformed bulk sample that includes regions of high and low dislocation density, a critical dislocation density can be defined so that the diffusion flux through these two regions is the same. To calculate the critical density, an fcc cross section area is calculated such that its flux is equal to the flux through the dislocation cross section area depicted in Fig. 2. Dividing the number of dislocations (1) by the sum of these two cross section areas gives the corresponding critical dislocation density, which is depicted in Fig. 7(b). The deformed bulk, having this density, is assumed to contain only parallel screw dislocations and no other debris. The calculated dislocation density therefore is a threshold, above which diffusion through dislocations would be the dominant contributor to overall diffusion. The dislocation density of a well-annealed fcc crystal is about 10^{10} m^{-2} [59], while a recent plastic deformation study suggested a saturation density of about 3×10^{14} to 2×10^{15} m^{-2} in Ni, depending on the measuring method [60]. The well-annealed value is significantly less than the theoretical ones plotted in the figure, but the necessary density could be present in the deformed sample at low temperatures up to around 700 K. Theory and experiment agree that pipe diffusion could be the primary means of mass transport that occurs in emerging ultrafine-grain (UFG) materials that have dislocation densities at these levels, though the experimentally suggested threshold density is much lower. The disagreement between experimental and calculated diffusion coefficients for pipe diffusion [reflected in Fig. 7(a)] results in the separation of the two curves in Fig. 7(b) by several orders of magnitude. If a correctional term was applied to account for this, these two lines would intercept one another at high temperature. Another reason for the disagreement between reported thresholds is the significantly greater experimentally reported activation energy for fcc diffusion (seen in Table II), which causes the experimental curve in Fig. 7(b) to decrease more sharply than the theoretical curve as temperature decreases. (The comparison of data from the two experimental studies is not perfect due to the different methodologies and extrapolation of higher temperature Arrhenius parameters to calculate D values near room temperature.)

Considering Figs. 6 and 7(b), pipe diffusion is not the dominant isotropic bulk diffusion mechanism in well-annealed fcc Ni, which is in line with expectations. However, the local effects of pipe diffusion on deformation (i.e., climb and creep mechanisms) will be quite significant, since pipe diffusion consistently provides greater diffusivities than would otherwise exist in fcc Ni. One could expect pipe diffusion to be the rate limiting process for diffusion-controlled dislocation motion over a wide range of dislocation densities. Also, these results provide support for the proposed idea that pipe diffusion makes grain boundary sliding possible in these UFGs at low temperatures where deformation is assumed to be negligible in traditional metals [61].

IV. CONCLUSION

Pipe diffusion was analyzed along a partial screw dislocation in fcc Ni using a first-principles approach. Diffusion coefficients describing monovacancy-facilitated diffusion along a dislocation line were calculated for a temperature range of 300–1400 K. These values are consistently significantly higher than those calculated in crystalline fcc Ni, even when correlation effects made mass transport along the dislocation core inefficient at low temperatures. This diffusion depends significantly on vacancies hopping to and from stacking fault sites as well as those that were adjacent to the core. Comparisons were made to experimental findings, and limitations of directly comparing the two were discussed. Pipe diffusion is likely to contribute to creep and climb mechanisms that involve mass transport near or along dislocations. Finally, integrated fluxes across the core structure were calculated to assess the critical dislocation density required to exceed conventional (bulk) mass transport. We observe that the required dislocation densities are achieved in stage II–III deformed metals and are also likely to be encountered in ultrafine grain materials at low temperatures.

ACKNOWLEDGMENTS

This research was supported in part by Air Force agreement FA8650-12-2-7248 and the Defense Associated Graduate Student Innovators (DAGSI) program, and computer time from the DoD High Performance Computing Modernization Program at the Air Force Research Laboratory DoD Supercomputing Research Center (AFRL-DSRC).

[1] O. Ruano, A. Miller, and O. Sherby, Mater. Sci. Eng. **51**, 9 (1981).
[2] T. Carter, Eng. Fail. Anal. **12**, 237 (2005).
[3] B. Arab, S. Sanjabi, and A. Shokuhfar, Mater. Lett. **65**, 712 (2011).
[4] R. Sundaresan, A. C. Raghuram, R. M. Mallya, and K. I. Vasu, Powder Metall. **39**, 138 (1996).
[5] M. Legros, G. Dehm, E. Arzt, and T. J. Balk, Science **319**, 1646 (2008).
[6] M. Garbrecht, B. Saha, J. L. Schroeder, L. Hultman, and T. D. Sands, Sci. Rep. **7**, 46092 (2017).
[7] M. Wuttig and H. K. Birnbaum, Phys. Rev. **147**, 495 (1966).
[8] R. F. Canon and J. P. Stark, J. Appl. Phys. **40**, 4366 (1969).
[9] J. Čermák and Z. Čochnář, Mater. Sci. Eng. A **174**, 9 (1994).
[10] H. Bakker, Phys. Status Solidi B **28**, 569 (1968).
[11] K. Maier, H. Mehrer, E. Lessmann, and W. Schüle, Phys. Status Solidi B **78**, 689 (1976).
[12] M. Feller-Kniepmeier, M. Gruendler, and H. Helfmeier, Z. Metallkd. **67**, 533 (1976).
[13] A. R. Wazzan, J. Appl. Phys. **36**, 3596 (1965).
[14] A. Janotti, M. Krčmar, C. L. Fu, and R. C. Reed, Phys. Rev. Lett. **92**, 085901 (2004).
[15] M. Krčmar, C. L. Fu, A. Janotti, and R. C. Reed, Acta Mater. **53**, 2369 (2005).
[16] C. Z. Hargather, S.-L. Shang, Z.-K. Liu, and Y. Du, Comput. Mater. Sci. **86**, 17 (2014).
[17] D. R. Alfonso and D. N. Tafen, J. Phys. Chem. C **118**, 22221 (2014).
[18] H. Wu, T. Mayeshiba, and D. Morgan, Sci. Data **3**, 160054 (2016).
[19] G. P. P. Pun and Y. Mishin, Acta Mater. **57**, 5531 (2009).
[20] R. C. Picu and D. Zhang, Acta Mater. **52**, 161 (2004).
[21] J. Huang, M. Meyer, and V. Pontikis, Phys. Rev. Lett. **63**, 628 (1989).
[22] X. Zhang and G. Lu, Phys. Rev. B **82**, 012101 (2010).
[23] C. Woodward and S. I. Rao, Phys. Rev. Lett. **88**, 216402 (2002).
[24] A. M. Z. Tan, D. R. Trinkle, and C. Woodward (unpublished).
[25] G. Kresse and J. Hafner, Phys. Rev. B **47**, 558 (1993).
[26] G. Kresse and J. Hafner, Phys. Rev. B **49**, 14251 (1994).
[27] G. Kresse and J. Furthmüller, Comput. Mater. Sci. **6**, 15 (1996).
[28] G. Kresse and J. Furthmüller, Phys. Rev. B **54**, 11169 (1996).
[29] P. E. Blöchl, Phys. Rev. B **50**, 17953 (1994).
[30] G. Kresse and D. Joubert, Phys. Rev. B **59**, 1758 (1999).
[31] M. Methfessel and A. T. Paxton, Phys. Rev. B **40**, 3616 (1989).
[32] C. Woodward, A. van de Walle, M. Asta, and D. Trinkle, Acta Mater. **75**, 60 (2014).
[33] J. E. Sinclair, P. C. Gehlen, R. G. Hoagland, and J. P. Hirth, J. Appl. Phys. **49**, 3890 (1978).
[34] S. Rao, C. Hernandez, J. P. Simmons, T. A. Parthasarathy, and C. Woodward, Philos. Mag. A **77**, 231 (1998).
[35] C. Woodward, D. R. Trinkle, L. G. Hector, Jr., and D. L. Olmsted, Phys. Rev. Lett. **100**, 045507 (2008).
[36] A. M. Z. Tan and D. R. Trinkle, Phys. Rev. E **94**, 023308 (2016).
[37] A. Hunter, R. F. Zhang, and I. J. Beyerlein, J. Appl. Phys. **115**, 134314 (2014).
[38] See Supplemental Material at http://link.aps.org/supplemental/10.1103/PhysRevMaterials.3.033605 for convergence testing information and methodology details.
[39] H. Jónsson, G. Mills, and K. M. Jacobsen, in *Classical and Quantum Dynamics in Condensed Phase Simulations*, edited by B. J. Berne, G. Ciccotti, and D. F. Coker (World Scientific, Singapore, 1998), Chap. 16, p. 385.
[40] G. Henkelman, B. P. Uberuaga, and H. Jónsson, J. Chem. Phys. **113**, 9901 (2000).
[41] G. Henkelman and H. Jónsson, J. Chem. Phys. **113**, 9978 (2000).
[42] D. Sheppard, R. Terrell, and G. Henkelman, J. Chem. Phys. **128**, 134106 (2008).
[43] M. Mantina, Y. Wang, L. Q. Chen, Z. K. Liu, and C. Wolverton, Acta Mater. **57**, 4102 (2009).
[44] T. Garnier, V. R. Manga, D. R. Trinkle, M. Nastar, and P. Bellon, Phys. Rev. B **88**, 134108 (2013).
[45] M. Glicksman, *Diffusion in Solids: Field Theory, Solid-State Principles, and Applications* (John Wiley and Sons, New York, 2000).
[46] G. H. Vineyard, J. Phys. Chem. Solids **3**, 121 (1957).
[47] A. Voter, in *Radiation Effects in Solids*, edited by K. E. Sickafus, E. A. Kotomin, and B. P. Uberuaga (Springer, Berlin, 2007), Vol. 235, Chap. 1, pp. 1–23.
[48] A. B. Bortz, M. H. Kalos, and J. L. Lebowitz, J. Comput. Phys. **17**, 10 (1975).

[49] C. C. Battaile, Comput. Methods Appl. Mech. Eng. **197**, 3386 (2008).
[50] N. Takahashi, T. Mizoguchi, T. Tohei, K. Nakamura, T. Nakagawa, N. Shibata, T. Yamamoto, and Y. Ikuhara, Mater. Trans. **50**, 1019 (2009).
[51] A. Stukowski, Modell. Simul. Mater. Sci. Eng. **18**, 015012 (2010).
[52] A. Stukowski and K. Albe, Modell. Simul. Mater. Sci. Eng. **18**, 085001 (2010).
[53] A. Stukowski, V. V. Bulatov, and A. Arsenlis, Model. Simul. Mater. Sci. Eng. **20**, 085007 (2012).
[54] R. W. Balluffi and A. V. Granato, in *Dislocations in Solids*, edited by F. R. N. Nabarro (North-Holland, Amsterdam, 1979), Vol. 4, Chap. 13.
[55] K. Compaan and Y. Haven, Trans. Faraday Soc. **52**, 786 (1956).
[56] T. R. Mattsson and A. E. Mattsson, Phys. Rev. B **66**, 214110 (2002).
[57] A. Metsue, A. Oudriss, J. Bouhattate, and X. Feaugas, J. Chem. Phys. **140**, 104705 (2014).
[58] M. R. Sørensen, Y. Mishin, and A. F. Voter, Phys. Rev. B **62**, 3658 (2000).
[59] P. M. Anderson, J. P. Hirth, and J. Lothe, *Theory of Dislocations* (Cambridge University Press, Cambridge, 2016), Vol. 3.
[60] Y. Miyajima, T. Ueda, H. Adachi, T. Fujii, S. Onaka, and M. Kato, IOP Conf. Ser.: Mater. Sci. Eng. **63**, 012138 (2014).
[61] L. S. Toth and C. Gu, Mater. Charact. **92**, 1 (2014).